

ACCEPTED MANUSCRIPT

Design and analysis of a large-range precision micromanipulator

To cite this article before publication: Xiantao Sun *et al* 2019 *Smart Mater. Struct.* in press <https://doi.org/10.1088/1361-665X/ab4413>

Manuscript version: Accepted Manuscript

Accepted Manuscript is “the version of the article accepted for publication including all changes made as a result of the peer review process, and which may also include the addition to the article by IOP Publishing of a header, an article ID, a cover sheet and/or an ‘Accepted Manuscript’ watermark, but excluding any other editing, typesetting or other changes made by IOP Publishing and/or its licensors”

This Accepted Manuscript is © 2019 IOP Publishing Ltd.

During the embargo period (the 12 month period from the publication of the Version of Record of this article), the Accepted Manuscript is fully protected by copyright and cannot be reused or reposted elsewhere.

As the Version of Record of this article is going to be / has been published on a subscription basis, this Accepted Manuscript is available for reuse under a CC BY-NC-ND 3.0 licence after the 12 month embargo period.

After the embargo period, everyone is permitted to use copy and redistribute this article for non-commercial purposes only, provided that they adhere to all the terms of the licence <https://creativecommons.org/licenses/by-nc-nd/3.0>

Although reasonable endeavours have been taken to obtain all necessary permissions from third parties to include their copyrighted content within this article, their full citation and copyright line may not be present in this Accepted Manuscript version. Before using any content from this article, please refer to the Version of Record on IOPscience once published for full citation and copyright details, as permissions will likely be required. All third party content is fully copyright protected, unless specifically stated otherwise in the figure caption in the Version of Record.

View the [article online](#) for updates and enhancements.

Design and analysis of a large-range precision micromanipulator

Xiantao Sun¹, Weihai Chen^{1,*}, Wenjie Chen^{1,*}, Shuhao Qi²,
Wang Li², Cungang Hu¹, and Jun Tao¹

¹School of Electrical Engineering and Automation, Anhui University, Hefei, China

²School of Automation Science and Electrical Engineering, Beihang University, Beijing, China

E-mail: whchenbuaa@126.com (Weihai Chen), wjiechen@yahoo.com.sg (Wenjie Chen)

Keywords: Scott-Russell mechanism, position/force sensing, large operation range, micromanipulator.

Abstract.

This paper proposes the design of a novel flexure-based micromanipulator dedicated to micro/nano manipulation and assembly tasks. The micromanipulator can provide a millimeter-scale operation range with high accuracy by the piezoelectric actuation. It is mainly enabled by a novel mechanical structure with a multi-stage amplification mechanism and a dual-stage grasping end-effector. Strain-type position and force sensors are integrated to detect the output motion and grasping force of the micromanipulator, respectively. Analytical models are established to predict the kinematic, static and dynamic characteristics, with further verification through finite element analysis. Finally, the principle prototype is fabricated, with which strain-gauge calibration and performance tests are conducted. Experimental results demonstrate that the micromanipulator has an operation range of 1 mm, high displacement/force resolution, and large grasping force. All of the results indicate the excellent characteristics of the developed micromanipulator that is expected to be applied into practical industrial applications.

Nomenclature

d_i, d_o	input/output displacement	δ_i	deformation of leaf-type flexure
R_i	motion amplification ratio	T, V	kinematic/potential energy
v_i	velocity	F_i, F_g	input/grasping force
L_i	linkage length	M_a	mechanical advantage
$\alpha, \beta, \gamma, \theta, \varphi$	linkage position angle	V_i	voltage
\mathbf{p}, \mathbf{e}	position/unit vector	I_i	moment of inertia
s	initial distance of two jaws	σ_y	yield strength
ϕ	maximum size of object	K_j	stiffness of flexure joint
r_i, b	radius/width of flexure joint	s	gauge factor
ψ_i	angle deformation of flexure joint	w_i	angular velocity
t_i	minimum thickness of flexure joint	K, M	equivalent stiffness/mass
E	Young's modulus	f	working mode frequency

1. Introduction

With the rapid development of micromachining and microscopic techniques, the operation objects are downsized for emerging microscale manipulations [1]. Automated micromanipulator is a typical tool that can be utilized to implement the pick-hold-release operation of small-scaled and fragile objects. It has been widely applied in the fields of micro/nano surgery, optical fiber alignment, biological cell manipulation, micro component assembly, etc [2]-[5]. Among above applications, two critical challenges for micromanipulators are large grasping range and high accuracy, which mainly depend on actuation principles, sensing techniques, and flexure-based motion amplification mechanisms (FMAMs). As a result, there is an urgent need to design a novel micromanipulator with excellent characteristics to deal with various micro/nano manipulation and assembly tasks.

So far, a variety of micromanipulators with different actuators have been reported in the literature [6]-[10]. For instance, electrostatically actuated MEMS grippers have been developed with the operation range of about 100 μm , and the grasping forces are very small and less than 1mN in [11]-[13]. A few MEMS grippers adopt electrothermal actuators, which suffer from high operation temperature and high power consumption in [14], [15]. Some distributed-compliance precision grippers driven by the voice coil motor (VCM) have been well studied in [16], [17]. The VCM has a large motion range with high precision, but it typically has a small driving force [18], [19]. Shape-memory-alloy (SMA) actuated micromanipulators have been reported in [20], [21], but the drawbacks of short fatigue life and slow response speed of SMA restrict their wide applications. In particular, as compared with the aforementioned actuators, the stack piezoelectric ceramic actuator (SPCA) without encapsulation shell is more attractive in precision positioning and manipulating systems owing to its merits of small size suitable for compact design, nanometer resolution, large driving force, and high dynamic response. Recently, it has found a number of SPCA-actuated micromanipulators with different mechanical structures [22]-[26]. To the best of our knowledge, few miniature SPCA-actuated micromanipulators can achieve an operation range larger than 1 mm with high resolution, which is related to the limited motion amplification of the micromanipulator structure. However, to better adapt different objects with various sizes, it is desirable and challenging to design such a large-range precision SPCA-actuated micromanipulator with a novel mechanical structure, which can also reduce the demand for high precision micromanipulator positioning systems indirectly.

Besides operation ranges, the capacity of sensing grasping force during manipulation is another criterion for micromanipulators. The main reason for this is that the manipulated micro objects usually have very small sizes and are sensitive to external forces. In the literature, many sensing methods have been proposed. For instance, the capacitive force sensor is integrated into the MEMS gripper to measure the grasping or interaction force based on the capacitance change in [13], [27]. Similar sensing techniques (e.g., electrothermal, piezoelectric, and piezoresistive, etc) are also used in

the measurement of micromanipulators in [11], [28]-[30]. Micro-optical technique is utilized to detect the action force for micro-robots in [31]. It is worth mentioning that a novel compliant constant-force mechanism is utilized to guarantee the grasping force instead of a force sensor in [10], [32]. The computer vision has been successfully utilized to detect the position and grasping force of micromanipulators in [33]. In addition, the self-sensing technique is proposed recently and it mainly aims at the specific smart materials that can be used as a sensor and an actuator simultaneously [20], [34], [35]. However, for the macro-scale micromanipulator [16], [22], [23], the strain gauge is more suitable to provide a low-cost, accurate and reliable detection method for position/force sensing in despite of the bonding difficulty and thermal sensitivity, and meanwhile it increases the integration level of the micromanipulator.

However, the existing SPCA-actuated micromanipulators have a small operation range due to the limited motion amplification from FMAM. The motivation of this paper is to design a large-range precision micromanipulator with integrated position/force sensing. A novel mechanical structure is designed to accomplish a large operation range of 1 mm. Specifically, a multi-stage amplification mechanism based on the improved Scott-Russell (SR) mechanism is utilized to amplify the limited stroke of SPCA. Moreover, a dual-stage end-effector is integrated into the mechanical structure to further extend the operation range on the basis of its own FMAM without reducing the resolution. Two strain gauges are attached on the corresponding flexure units to detect the output motion and grasping force of the micromanipulator, respectively.

The main contribution of this paper is the design of a large-range SPCA-actuated micromanipulator with the submicrometer displacement resolution and millinewton force resolution. In the following parts of this paper, Section 2 describes three novel FMAMs based on the SR mechanism, a multi-stage grasping end-effector, and the resulted structural design of a novel SPCA-actuated micromanipulator. In Section 3, the kinematic, static and dynamic models are established. Then, the performance evaluation is carried out by finite element analysis (FEA) in Section 4. After that, the principle prototype is fabricated in Section 5 along with performance testing and some automated grasping manipulations. Finally, conclusions are summarized in Section 6.

2. Mechanical Design

2.1. Motion Amplification Mechanisms

Throughout commercial SPCA products, the significant drawback of SPCA is the limited stroke, which is about 0.1% of its length. Hence, various FMAMs are utilized to amplify the limited stroke of SPCA in the SPCA-actuated positioning and manipulating systems. Up to now, several typical FMAMs have been reported, namely, leverage mechanism [7], [8], [36], bridge-type mechanism [37]-[39], and SR mechanism [40], [41], etc. However, in comparison with the first two FMAMs, SR mechanism has attracted much more attention due to its advantages of straight-line motion, compact physical

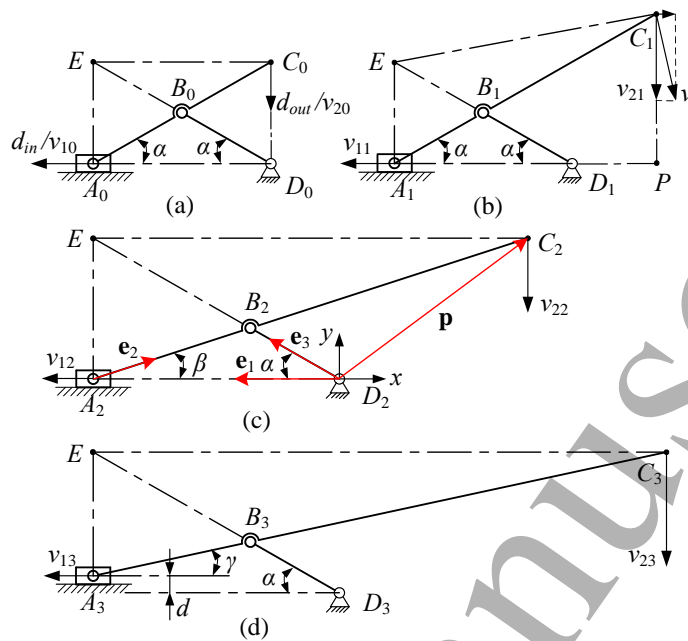


Figure 1. PRBMs of (a) original SR mechanism and (b) ~ (d) its three improved mechanisms #1, #2 and #3.

size, and simple structure [41]. To achieve a much larger operation range than existing SPCA-actuated micromanipulators for handling objects ranging from micrometer to millimeter size, three improved SR mechanisms are first proposed and their pseudo-rigid-body models (PRBMs) are shown in Fig. 1.

Referring to Fig. 1(a), the motion amplification ratio (MAR) of the original SR mechanism is calculated by the relationship between the input variables (displacement d_i and velocity v_{10}) and the output variables (displacement d_o and velocity v_{20}) as

$$R_0 = \frac{\partial d_o}{\partial d_i} = \frac{\partial d_o / \partial t}{\partial d_i / \partial t} = \frac{v_{20}}{v_{10}} = \cot \alpha \quad (1)$$

which indicates that the magnitude of MAR is governed by the position angle α of link D_0B_0 or A_0C_0 . However, the angle only keeps decreasing for the sake of a larger MAR, which will undoubtedly increase the difficulty of design and machining, and at this moment the MAR is more sensitive to machining error.

Intuitively, increasing the length of link B_0C_0 can extend the arm length of velocity at point C_0 relative to the instantaneous center E , and the resulted improved mechanism #1 is described by Fig. 1(b). However, this improvement unfortunately leads to an inevitable parasitic motion along the horizontal direction, which cannot be eliminated by simply extending the length of link B_1C_1 . Hence, in order to eliminate the undesirable parasitic motion, a new improved mechanism #2 is proposed in Fig. 1(c) by changing the position angle β and the length of link A_2C_2 simultaneously. In addition, changing the centric slider-crank mechanism $D_2B_2A_2$ into an offset slider-crank mechanism $D_3B_3A_3$

Table 1. Structural parameters of four SR mechanisms.

Symbol	Value	Unit	Symbol	Value	Unit
α	26.6	$^{\circ}$	$L_{D_2A_2}$	25	mm
$L_{D_iB_i}$	11.2	mm	γ	14.9	$^{\circ}$
$L_{B_1C_1}$	22.4	mm	d	1	mm

with the offset distance of d can generate a similar mechanism #3 shown in Fig. 1(d). The MARs of three improved SR mechanisms are obtained as

$$R_1 = v_{21}/v_{11} = \cot \alpha + L_{D_1P}/L_{EA_1} \quad (2)$$

$$R_2 = v_{22}/v_{12} = \cot \beta \quad (3)$$

$$R_3 = v_{23}/v_{13} = \cot \gamma \quad (4)$$

Assume that the length and position angle of link D_iB_i ($i = 0, 1, 2$, and 3) hold, and the links D_2A_2 and D_3A_3 have the same horizontal projection length. It is observed that the three improved mechanisms significantly increase the MAR relative to the original one, and the mechanism #3 possesses a larger MAR than the mechanism #2.

Referring to Fig. 1(c), two position-loop equations can be written for kinematics analysis as follows:

$$\mathbf{p} = L_{D_iA_i}\mathbf{e}_1 + L_{A_iC_i}\mathbf{e}_2 = L_{D_iB_i}\mathbf{e}_3 + \lambda L_{A_iC_i}\mathbf{e}_2 \quad (5)$$

where $\mathbf{p} = [x \ y]^T$ is the position vector of output point C_i , \mathbf{e}_1 , \mathbf{e}_2 , and \mathbf{e}_3 are the unit vectors pointing along D_iA_i , A_iC_i , and D_iB_i , respectively, and λ is length coefficient of link B_iC_i relative to link A_iC_i and satisfies $\lambda = L_{B_iC_i}/L_{A_iC_i}$ ($i = 1, 2$, and 3).

Rearranging these items of Eq. (5), dot-multiplying with each other, and solving them derives the solutions for the kinematics problem as follows:

$$\mathbf{p}^T\mathbf{p} = \frac{\lambda}{\lambda-1}L_{D_iA_i}^2 - \frac{1}{\lambda-1}L_{D_iB_i}^2 + \lambda L_{A_iC_i}^2 \quad (6)$$

$$\mathbf{p}^T\mathbf{e}_1 = \frac{2\lambda-1}{2(\lambda-1)}L_{D_iA_i} - \frac{1}{2(\lambda-1)} \cdot \frac{L_{D_iB_i}^2}{L_{D_iA_i}} + \frac{\lambda-1}{2} \cdot \frac{L_{A_iC_i}^2}{L_{D_iA_i}} \quad (7)$$

where only the positive solutions in Eqs (6) and (7) are taken into account to avoid the singular configuration with the links A_iC_i and B_iD_i overlapped.

To further evaluate the motion characteristics of three improved SR mechanisms quantitatively, the geometric parameters are given as listed in Table 1. The influence of the main motion on the parasitic motion is analyzed and summarized in Fig. 2. It is observed that the mechanism #1 has the largest parasitic motion while the

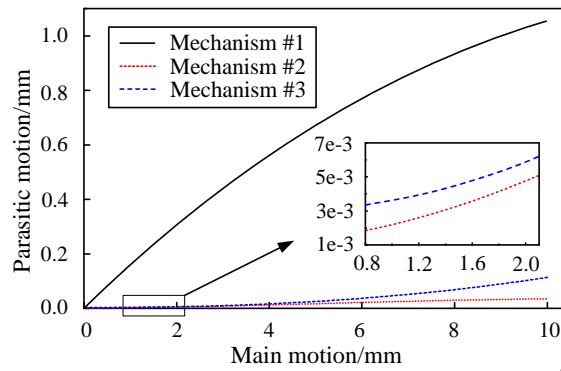


Figure 2. Parasitic motion versus main motion of three improved SR mechanisms.

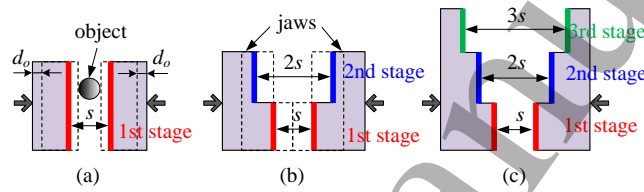


Figure 3. Three grasping manners of end-effectors: (a) single-stage, (b) dual-stage, and (c) three-stage.

mechanism #2 has the smallest parasitic motion among them. The coupling rates of the mechanisms #2 and #3 are 0.3% and 1% respectively when the main motion reaches up to about 10 mm close to their singular configurations. Thus, it can be predicted that the mechanism #2 has promising applications as a linear guiding module in robotic mechanisms. However, considering that the flexure-based mechanism usually has a small motion within the micrometer level, the mechanism #3 is selected as the FMAM of the micromanipulator due to its larger MAR. Even so, its coupling rate is only 0.35% at the output motion of 1 mm and can be ignored completely.

2.2. Multi-stage Grasping End-effector

Generally, the operation objects have irregular geometrical shapes in different micro/nano manipulation and assembly tasks. The single-stage parallel grasping manner is usually adopted as grasping motion modulation in most micromanipulators as shown in Fig. 3(a) [7], [8], [21]-[25]. It can provide a pure translational motion of the end-effector for a firm and reliable grasping process.

It is assumed without loss of generality that the clearances between the operation object and the two end-effector jaws are identical. Referring to Fig. 3(a), after a particular input displacement d_i from the SPCA, each jaw translates over an output distance of d_o determined by the FMAM MAR. Then, they contact the object. The operation range of the micromanipulator can be expressed as

$$0 < \phi \leq s \quad \text{for} \quad 2d_o \geq s \quad (8)$$

Table 2. Structural parameters (mm) of the micromanipulator.

Symbol	Value	Symbol	Value
L_0	7	L_g	10
L_1	3.8	t_g	0.3
L_2	5	t_0	0.2
L_3	25	b	6
L_4	10	r_A, r_E	1
L_5	11.9	r_C, r_H	2
L_6	5	$r_I \sim r_L$	2.5
L_7	35	r_B, r_D, r_F, r_G	0.4

$$s - 2d_o \leq \phi \leq s \quad \text{for} \quad 2d_o < s \quad (9)$$

where ϕ is the maximum size of the object along the grasping direction, and s represents the initial distance of two jaws.

Hence, in view of Eqs. (8) and (9), in order to take full advantage of the grasping clearance between two jaws to obtain a full operation range of $[0, s]$, the precondition of $2d_o \geq s$ should be guaranteed. However, the allowable maximum displacement of the end-effector is restricted by the yield stress of the material and cannot be infinitely amplified by the FMAM as a consequence. Besides, a large MAR can easily leads to poor dynamic property of the FMAM. They are the crucial factors that limit the operation range of existing SPCA-actuated micromanipulators.

Aiming at the above problem, to realize a large operation range with a limited end-effector displacement, the concept of multi-stage grasping manner with multi-pair jaws is proposed as shown in Figs. 3(b) and 3(c), where different jaws are prepared for grasping different sized objects, i.e., the i th-stage end-effector for smaller-sized objects and the j th-stage one for larger-sized objects ($j > i$). Note that the end-effector clearances has a linear increment relation. Under the precondition of $2d_o \geq s$, taking the dual-stage end-effector with two-pair jaws for instance, the first-stage one with a smaller clearance of s can be closed completely as shown in Fig. 3(b) while the clearance of the second-stage one changes from $2s$ to s , and the operation range can be divide into two intervals of $(0, s]$ and $[s, 2s]$ for the first- and second-stage end-effector, respectively. However, the two segmented operation ranges can form a continuous, closed and more larger range of $(0, 2s]$ that is twice as large as that of the single-stage end-effector. Similarly, the operation range of the three-stage end-effector is $(0, 3s]$, and so on. Different from existing micromanipulators, the proposed grasping manner with multi-pair jaws is a simple but effective way to provide another promising solution to the large-range grasping operation without the assistance of any FMAMs.

2.3. Mechanism Description

Motivated by the aforesaid advantages, a novel SPCA-actuated flexure-based micromanipulator is designed as shown in Fig. 4. It consists of a SPCA, a monolithic

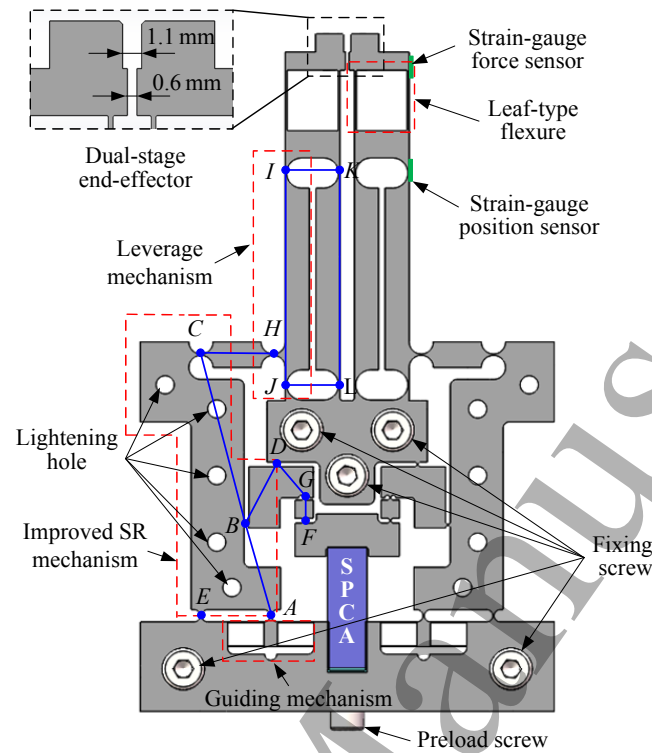


Figure 4. CAD model of the SPCA-actuated micromanipulator.

FMAM with a dual-stage end-effector, two strain gauges for position and force sensing, and several fixing and preload screws. The main structural parameters (see Fig. 5) of the micromanipulator are described in Table 2. The limited stroke of SPCA is amplified by the FMAM with a MAR of R . A guiding mechanism is introduced to guarantee the motion linearity and stability of the improved SR mechanism. Leaf-type parallelogram flexure (LTPF) is employed to provide the parallel grasping of the end-effector. To achieve better output characteristics, the SPCA requires to be preloaded, which will result in the decrease of the end-effector clearance indirectly. In view of this point, the initial dual-stage clearances of the end-effector are set to 0.6 mm and 1.1 mm, respectively. The redundant clearance (0.1 mm) of each-pair jaw is reserved for the clearance loss and will be eliminated through the adjustable preload screw. Thus, the micromanipulator can provide an operation range of $(0, 1 \text{ mm}]$ under a sufficient input motion. Additionally, without changing stress distribution, some lightening holes are symmetrically distributed in the two SR mechanisms. Meanwhile, combined with the addition of an extra supporting flexure joint E located at the instantaneous center of link ABC depicted in Fig. 1(d), a good dynamic behavior of the micromanipulator can be achieved. Since flexure joint is not a strict single-DOF joint due to its particular compliance in other directions, the joint E has a negligible effect on the motion characteristic of the SR mechanism, which has been validated by the FEA simulation. For the convenience of installation and measurement, the position strain gauge is attached on the flexure joint of the leverage mechanism, and the force strain gauge

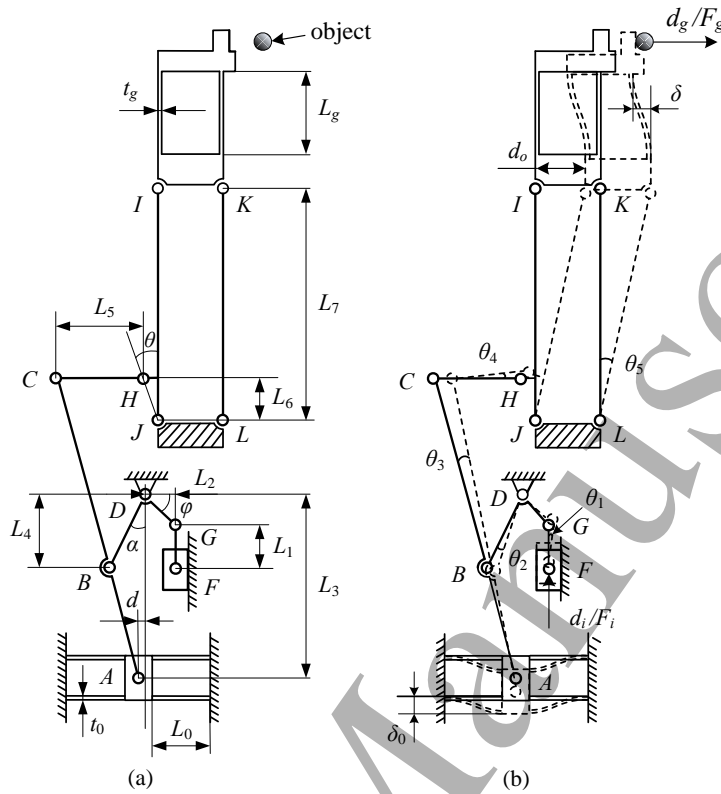


Figure 5. PRBM of the SPCA-actuated micromanipulator: (a) schematic diagram and (b) displacement diagram.

is glued on the LTPF end, as indicated in Fig. 4. Due to the symmetrical structure, the unilateral measurement is sufficient. The entire micromanipulator is installed on a support base through five fixing screws.

3. Modeling and Analysis

In this section, the kinematics, statics, and dynamics analysis of the developed micromanipulator are introduced in detail.

3.1. Kinematics Analysis

Assume that all flexure joints undergo pure bending deformations without any expansions or contractions, the equivalent model of the micromanipulator based on the PRBM approach can be obtained and shown in Fig. 5. After an input motion d_i and driving force F_i from SPCA, the end-effector jaw contacts the target object along with a translational motion d_g and grasping force F_g while the FMAM causes an output motion d_o . Regardless of the end-effector amplification, the MAR of the FMAM can be

IOP Publishing, Smart Materials and Structures, 2019

10

calculated as

$$R = d_o/d_i = R_{11} \cdot R_{22} \cdot R_{33} = \frac{L_4(L_3 \tan \alpha - d)}{L_2(L_3 - L_4)} \cdot \frac{L_3 - L_4}{L_4 \tan \alpha - d} \cdot \frac{L_7}{L_6} \quad (10)$$

where L_i ($i = 1 \sim 7$), α and d are the structural parameters of the FMAM (see Fig. 5). It is noted that the expression is composed of three terms that represent the three-stage amplification from the offset slider-crank mechanism ($F-G-D-B-A$), optimized SR mechanism ($D-A-B-C$), and leverage mechanism ($H-I-J$) of the FMAM, respectively.

According to the kinematics analysis, the angle increments $\theta_1 \sim \theta_5$ (see Fig. 5) of all links can be obtained and the deformations of all flexure joints are further derived as

$$\psi_F = \frac{d_i}{L_1 \cot \varphi} \quad (11)$$

$$\psi_G - \psi_F = \psi_D = \frac{d_i}{L_2} \quad (12)$$

$$\psi_A = \psi_E = \psi_B - \psi_D = \frac{R_1 d_i}{L_3 \tan \alpha - d} \quad (13)$$

$$\psi_I = \psi_J = \psi_K = \psi_L = \frac{R d_i}{L_7} \quad (14)$$

$$\psi_C - \psi_A = \psi_H - \psi_J = \frac{R_1 R_2 d_i}{L_5 \cot \theta} \quad (15)$$

where each variable ψ_j can be described as the linear relation of the input motion d_i , i.e., $\psi_j = \eta_j d_i$ ($j = A \sim L$) from the above equations.

3.2. Statics Analysis

Under the assumption of the pure bending deformations at flexure joints, only the torsional stiffness is taken into account to analyze the statics problem of the micromanipulator and is estimated by

$$K_{\theta i} = \frac{2Ebt_0^{5/2}}{9\pi r_i^{1/2}}, \quad i = A \sim H \quad (16)$$

$$K_{\theta j} = \frac{\sqrt{2}Ebt_0^{5/2}}{9\pi r_j^{1/2}}, \quad j = I \sim L \quad (17)$$

where E is the Young's modulus of the material, and b , t_0 , and r_i represent the width, minimum thickness, and radius of flexure joint i , respectively.

Referring to Fig. 4, each end-effector jaw is suspended by a LTPF while the guiding mechanism is composed of two parallel LTPFs, and their stiffness can be derived as

$$K_g = \frac{2Ebt_g^3}{L_g^3} \quad \text{and} \quad K_0 = \frac{4Ebt_0^3}{L_0^3} \quad (18)$$

where t_i and L_i ($i = 0$ and g) describe the thickness and length of the associated leaf-type flexures (see Fig. 5), respectively.

Neglecting the influence of gravity effect for the planar mechanism, the total potential energy of the micromanipulator arising from the elastic deformation of flexures is given as

$$V = 2 \left(\frac{1}{2} \sum_{i=A}^L K_{\theta i} \psi_i^2 + \frac{1}{2} K_0 \delta_0^2 + \frac{1}{2} F_g \delta \right) \quad (19)$$

where $\delta_0 = R_1 d_i$ and $\delta = d_o - d_g$ are the deformations of the two leaf-type flexures, respectively.

By applying the principle of virtual work, the total virtual work δW of the FMAM satisfies $\delta W = 0$ and can be given as

$$\delta W = - \frac{\partial V}{\partial d_i} \delta d_i + F_i \delta d_i \quad (20)$$

Consequently, the static model of the micromanipulator describing the force-deflection relationship can be derived as

$$\begin{aligned} F_i &= 2 \left(\sum_{i=A}^L K_{\theta i} \eta_i^2 + K_0 R_1^2 \right) d_i + 2 (R - d_g/d_i) F_g \\ &= K_i d_i + 2 (R - d_g/d_i) F_g \end{aligned} \quad (21)$$

where K_i denotes the input stiffness of the micromanipulator.

It is known that the grasping force is governed by the deformation $d_o - d_g$ at the specific stiffness K_g . Hence, its maximum value appears at the maximum of d_o and the minimum of d_g , i.e., $d_g = 0$, which means that the end-effector contacts the object at its initial position. In this case, the mechanical advantage of the micromanipulator, i.e., the ratio of the grasping force to the input force, is given as

$$M_a = \frac{F_g}{F_i} = \frac{RK_g}{K_i + 2R^2 K_g} \quad (22)$$

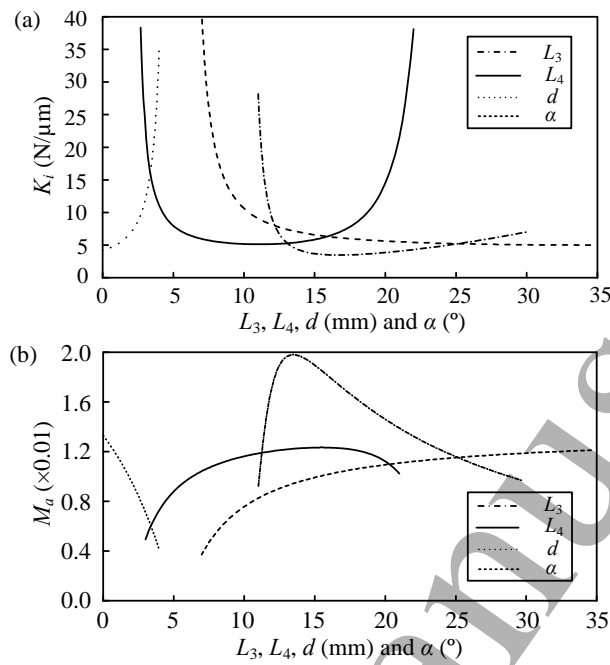


Figure 6. Influence of SR mechanism parameters on (a) the input stiffness and (b) the mechanical advantage of the micromanipulator.

Eqs. (21) and (22) indicate that the input stiffness and mechanical advantage are determined by the structural parameters of the FMAM. The influences of the SR mechanism parameters on the two key indicators are shown in Fig. 6. The input stiffness increases with d increasing and decreases as α increases, and a minimum value exists with the changes of L_3 and L_4 , but it is the opposite for the mechanical advantage. Finally, as listed in Table 1, the input stiffness is calculated as 5.08 N/μm, which is about 10.4% of the nominal SPCA stiffness. Hence, the SPCA can work properly and its motion loss is acceptable relative to the free stroke. Moreover, the mechanical advantage is very small on the order of 10^{-2} , which enables the precision force control of the micromanipulator.

To avoid the plastic deformations of the flexures, the maximum stress should keep within the yield strength σ_y of material. The allowable maximum deformations of flexure joints and leaf-type flexures can be calculated as follows:

$$\psi_i^{\max} = \frac{3\pi\sigma_y r_i^{1/2}}{4Et_0^{1/2}}, \quad i = A \sim H \quad (23)$$

$$\psi_j^{\max} = \frac{3\pi\sigma_y r_j^{1/2}}{2\sqrt{2}Et_0^{1/2}}, \quad j = I \sim L \quad (24)$$

$$\delta_0^{\max} = \frac{\sigma_y L_0^2}{3Et_0} \quad \text{and} \quad \delta_g^{\max} = \frac{\sigma_y L_g^2}{3Et_g} \quad (25)$$

To measure the output displacement and grasping force of the micromanipulator, each strain gauge together with three fixed resistors is employed to construct one quarter Wheatstone-bridge circuit for the sake of simplicity. The relationships between the output displacement d_o and grasping force F_g of the two sensors and the output voltages (V_o and V_g) of the two circuits can be derived respectively as follows:

$$d_o = \frac{6\pi r_I^{1/2} L_7}{\sqrt{2} t_0^{1/2} s V} V_o \quad (26)$$

$$F_g = \frac{8Ebt_g^2}{3L_g s V} V_g \quad (27)$$

where s is the gauge factor of the selected strain gauge, and V is the input voltage of the Wheatstone-bridge circuit. In addition, Eqs. (26) and (27) indicate the linear relationships between the output voltages and the measured values.

3.3. Dynamics Analysis

Without consideration of any local vibrations, the dynamic characteristic of the micromanipulator is analyzed along the working mode, where the input motion d_i is chosen as the generalized coordinate. The Lagrange's equation can be expressed based on the generalized coordinate d_i as

$$\frac{d}{dt} \left(\frac{\partial T}{\partial \dot{d}_i} \right) - \frac{\partial T}{\partial d_i} + \frac{\partial V}{\partial d_i} = F_i - RF_g \quad (28)$$

where V in Eq.(19) satisfies $\delta = 0$ at the working mode, and T denotes the total kinematic energy of the micromanipulator and is derived by

$$T = \frac{1}{2} m_i \dot{d}_i^2 + \sum_j I_j w_j^2 + m R_1^2 \dot{d}_i^2 + m_o R^2 \dot{d}_i^2 \quad (29)$$

where m_i , m , and m_o are the mass of the input end, guiding mechanism, and output end, respectively. I_j and w_j represent the moment of inertia with respect to its instantaneous center and angular velocity of link j ($j = FG, BG, AC, CH, IJ$, and KL), respectively.

The dynamic model of the micromanipulator is given as

$$M \ddot{d}_i + K d_i = F_i - RF_g \quad (30)$$

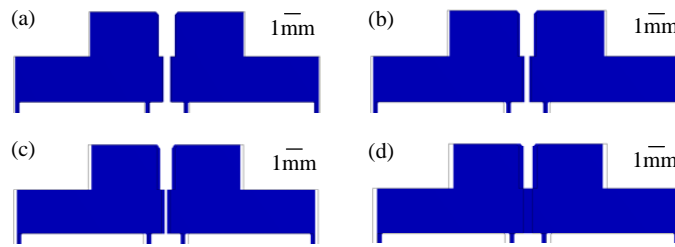


Figure 7. Motion simulations of the end-effector under different input displacements of (a) 2 μm , (b) 4 μm , (c) 6 μm , and (d) 9.7 μm .

where M and K represent the equivalent mass and stiffness respectively, and are given as

$$M = m_i + \frac{2I_{FG}}{(L_1 \cot \varphi)^2} + \frac{2I_{BG}}{L_2^2} + 2\left(\frac{R_1}{L_3 \tan \alpha - d}\right)^2 I_{AC} + 2\left(\frac{R_1 R_2}{L_5 \cot \theta}\right)^2 I_{CH} + \frac{4R^2 I_{KL}}{L_7^2} + 2mR_1^2 + 2m_o R^2 \quad (31)$$

$$K = K_i \quad (32)$$

Hence, the working mode frequency of the micromanipulator is obtained as

$$f = \frac{1}{2\pi} \sqrt{\frac{K}{M}} \quad (33)$$

4. Performance Evaluation

To evaluate the performance of the micromanipulator, FEA simulations are conducted using ANSYS software R15.0. After several iterations of improved designs and simulations, the main structural parameters of the micromanipulator are determined as shown in Table 1. The material parameters of the selected AL7075-T6 alloy are Young's modulus of 71.7 GPa, Poisson's ratio of 0.33, yield strength of 503 MPa, and density of 2810 kg/m³, respectively. The finite element model is meshed by the tetrahedron element, and the large-deflection simulation function is activated and the flexure units are refined for high simulation accuracy. In addition, the fixing holes are constrained completely.

First, the static performance of the micromanipulator is evaluated using the static structural analysis. The simulations are performed by applying a series of different input displacements to the input end of the micromanipulator. The true-scale motions of the end-effector are shown in Fig. 7, where the wireframe represents the undeformed position. The results show that the maximum displacement of one end-effector jaw is

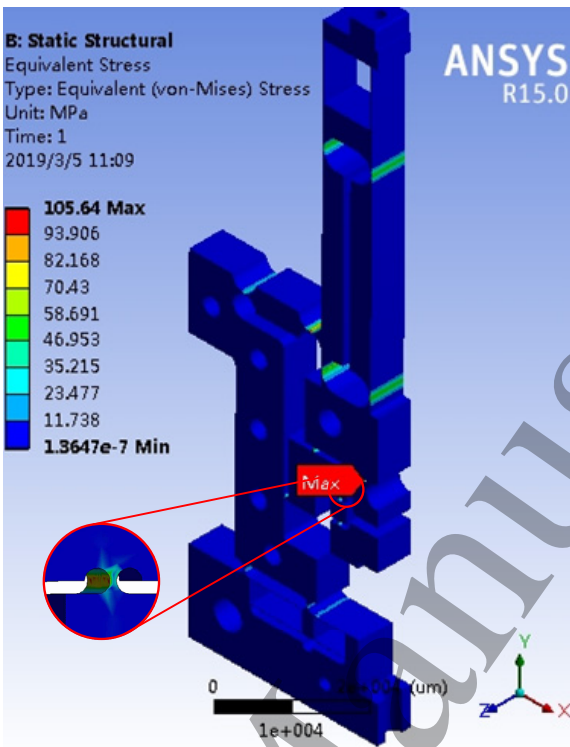


Figure 8. Stress distribution of the micromanipulator.

about 0.3 mm at the input displacement of 9.7 μm , which indicates that the MAR of the entire FMAM is 31. It is observed that the analytical model overestimates the MAR by 29.7%. Moreover, the MARs of the each-stage FMAM are 1.28, 3.67, and 6.61 respectively, and the motion loss of the second-stage amplification i.e., SR mechanism is minimum among the three, which benefits from the improved design. The overall stress distribution of the micromanipulator is shown in Fig. 8. To fully close the end-effector, the induced maximum stress occurs at the flexure joint G and is only 105.6 MPa, which is far less than the yield strength of the selected material. On the other hand, the force-deflection relationship is also analyzed by exerting several different input forces on the input end of the micromanipulator. The simulation results predict that the input stiffness and mechanical advantage are 4.27 N/ μm and 0.0112, which are close to the analytical results of 5.08 N/ μm and 0.0116, respectively. Moreover, the out-of-plane stiffness of 26.3 mN/ μm at the end-effector is sufficient to undergo the self weight of the operation object. It is seen from the simulation results that the micromanipulator is capable of adapting most micro objects with different physical properties in terms of size, fragility, and weight.

Second, the modal analysis is implemented to evaluate the dynamic performance of the micromanipulator. It is observed that the first mode shape is a local vibration mode that indicates the translations of the end-effector jaws along the same direction with a resonance frequency of 115 Hz, whereas the second mode (125.2 Hz) is the working mode of the micromanipulator. The simulation result coincides with the analytical result of

Table 3. Performance evaluation of the micromanipulator by analytical models and FEA simulations.

Performance	Analytical models	FEA simulations	Model error (%)
R_1	1.54	1.28	20.3
R_2	3.74	3.67	1.9
R_3	7	6.61	5.9
R	40.2	31	29.7
K_i (N/ μm)	5.08	4.27	19
M	0.0116	0.0112	3.6
f (Hz)	115.7	125.2	-7.6

115.7 Hz.

For the sake of clarity, the comparison results of analytical models and FEA simulations are summarized in Table 3. The model errors are mainly attributed to the assumption of single-DOF flexure joint for the analytical models. The model accuracy can be improved by the nonlinear modeling instead [42].

5. Experimental Tests

In this section, a prototype of the proposed micromanipulator is fabricated, and a series of experimental tests are performed to investigate its performance and demonstrate the aforementioned superiorities.

5.1. Prototype and Experimental Setup

Fig. 9 shows the experimental setup of the overall micromanipulator system. The prototype micromanipulator is fabricated from a piece of AL7075-T6 plate through the low-speed wire electrical discharge machining (LSWEDM) due to its high machining accuracy. A SPCA combined with a amplifier (model: AE0505D16F, BP303, from Thorlabs, Inc) is chosen to drive the micromanipulator. The SPCA can provide a maximum displacement of 17.4 μm with a nominal stiffness of 48.85 N/ μm . Its motion is measured by a capacitive sensor with a 1-nm resolution (model: C8-2.0 probe and CPL190 controller, from Lion Precision, Inc). The output displacement and grasping force of the micromanipulator are measured by two high-accuracy strain gauges respectively with a nominal resistance of 350 Ω and a gauge factor of about 2.1.

A National Instruments (NI) cDAQ-9184 with a four-channel NI-9237 simultaneous bridge module is employed to acquire analog voltage signals of two Wheatstone-bridge circuits constructed with two modules NI-9945. The strain-gauge position sensor is calibrated by a laser sensor with a 20-nm resolution within a 6-mm measuring range (model: LK-H020 from Keyence, Inc). To capture the operation process of the micromanipulator, a CCD camera (model: Manta G-125, from Allied Vision, Inc) with high pixel resolution is adopted. All experimental tests are performed on a vibration-

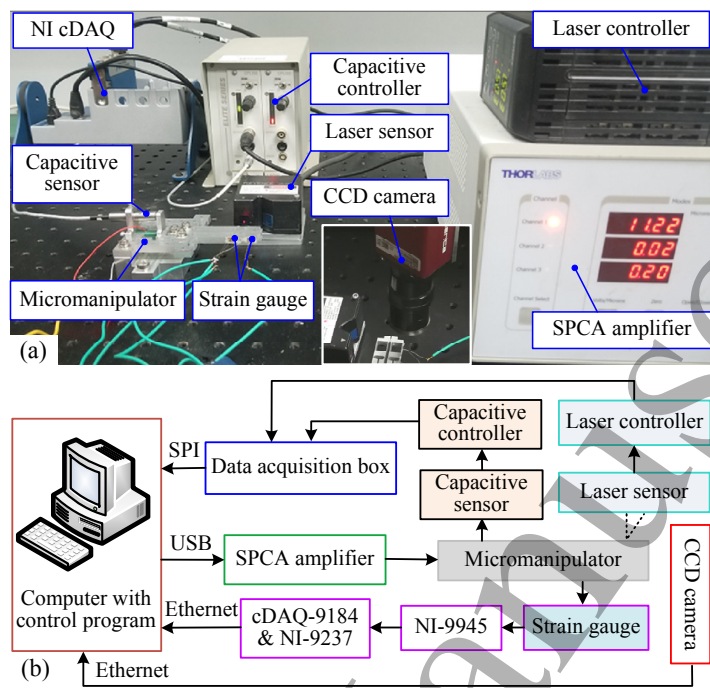


Figure 9. (a) Experimental setup and (b) schematic diagram of the overall micromanipulator system.

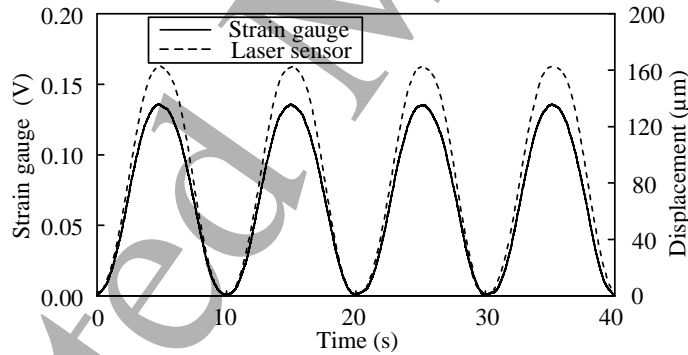


Figure 10. Calibration results of strain-gauge position sensor.

isolated platform to reduce the external disturbances.

5.2. Experiments and Discussions

Before conducting the testing experiments, the clearances of the dual-pair end-effector jaws are adjusted to 0.5 mm and 1 mm carefully through screwing the preload screws and observing the laser-sensor data. For strain gauges as sensors, the voltage signals should be converted into position/force signals manually, which are performed by comparing the voltage values with the reference position/force values [16]. For the calibration of strain-gauge position sensor, by applying a sinusoidal signal with a 80-V peak-to-peak (p-p) value and 0.1-Hz frequency to the SPCA, the output displacement of the micromanipulator is measured by the strain-gauge position sensor and laser sensor

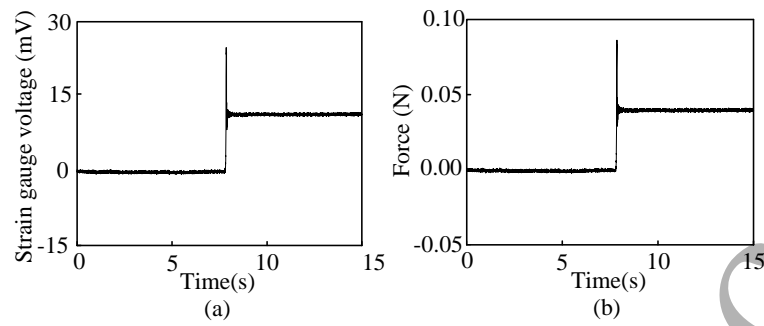


Figure 11. Calibration results of strain-gauge force sensor: (a) output voltage and (b) calibrated force.

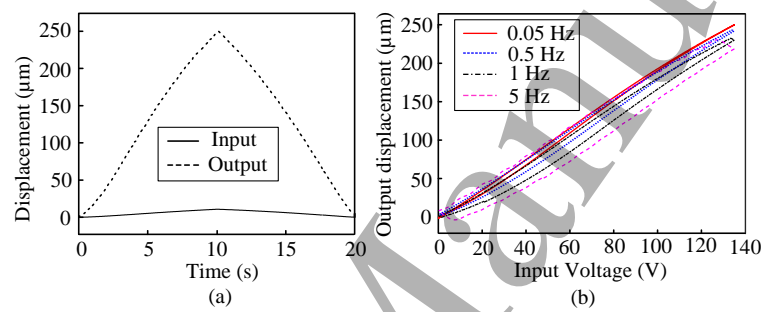


Figure 12. Test results of input and output displacements: (a) time history results and (b) hysteresis curves with different driving frequencies.

simultaneously. The calibration results are shown in Fig. 10, and the sensitivity of position sensor is calculated as $1.2 \mu\text{m}/\text{mV}$. For the calibration of strain-gauge force sensor, a known force of 39.2 mN from 4-g standard weight is applied to an end-effector jaw suddenly, the voltage signal of strain gauge is recorded, as shown in Fig. 11. It is seen that the steady voltage of the force sensor is 11 mV, which indicates the sensitivity of $3.56 \text{ mN}/\text{mV}$.

To confirm the grasping range and MAR of the micromanipulator, a triangular voltage with 135-V p-p value and low (0.05 Hz) frequency is applied to the SPCA, the input and output displacements are measured by the capacitive sensor and calibrated position sensor respectively in the open-loop control. It is found from Fig. 12(a) that the maximum displacement of one end-effector jaw is about $250 \mu\text{m}$ while the SPCA displacement is $8.5 \mu\text{m}$, which indicates the FMAM MAR of 29.4 close to the simulation result. At this moment, the first-stage end-effector are closed fully, and the clearance of the second-stage one changes from 1 mm to 0.5 mm. Thus, their grasping ranges are $(0, 0.5 \text{ mm}]$ and $[0.5 \text{ mm}, 1 \text{ mm}]$ respectively, and the total grasping range of the micromanipulator is $(0, 1 \text{ mm}]$. Besides, the hysteresis and nonlinearity behaviors are the inherent characteristics affecting the motion linearity of SPCA, and the FMAM makes them even worse. Fig.12(b) shows the relationship between the output displacement of the micromanipulator and the driving voltage with varying driving frequencies. It is observed that the hysteresis curve is dependent on the frequency (i.e.,

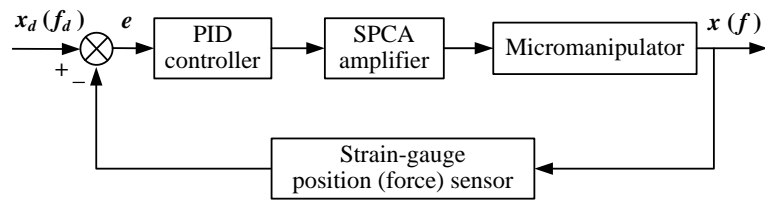


Figure 13. Block diagram of position/force close-loop controller.

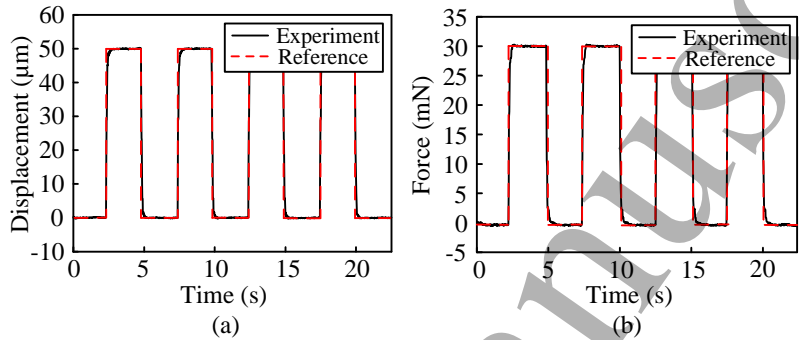


Figure 14. Square-wave motion tracking results of the given (a) displacement and (b) force values.

the higher frequency, the larger hysteresis), and meanwhile the output displacement decreases with the frequency. To further improve the linearity and repeatability of the micromanipulator, a popular proportional-integral-derivative (PID) controller is employed to reduce the adverse behaviors. The block diagram of position/force close-loop controller is shown in Fig. 13. Up to now, several hybrid position and force controls have been proposed for the fusion of both in [2], [5], [23]-[25]. The displacement and force trajectory tracking performance is firstly tested, and the square-wave motions with the amplitudes of 50- μm displacement and 30-mN force are shown in Fig. 14. Then, in order to measure the displacement and force resolution of the micromanipulator, the multi-step response experiments are conducted, and the results are shown in Fig. 15. It reveals the 0.6- μm displacement and 1.8-mN force resolution. It is noticeable that the resolution can be further enhanced by using half or full Wheatstone-bridge circuit.

To demonstrate the capability of the micromanipulator, the manipulation of objects with different sizes are implemented, respectively. Firstly, the micromanipulator is employed to grasp a metal wire with a diameter of about 320 μm . A trapezoidal voltage is applied to the SPCA, the output displacement and grasping force are measured by the strain-gauge position and force sensors, respectively. It is seen from Fig. 16 that the end-effector jaw is close to the object at a fast speed from t_1 to t_2 , and contacts the object at the time t_2 . Then, the grasping force begins to increases, and the speed of the output motion declines from t_2 to t_3 , which is induced by the high stiffness of the LTPF. After that, the end-effector holds the object, and the output displacement and grasping force remain unchanged from t_3 to t_4 . Finally, the end-effector releases the object after t_4 and completes an operation process. In addition, in order to further validate the

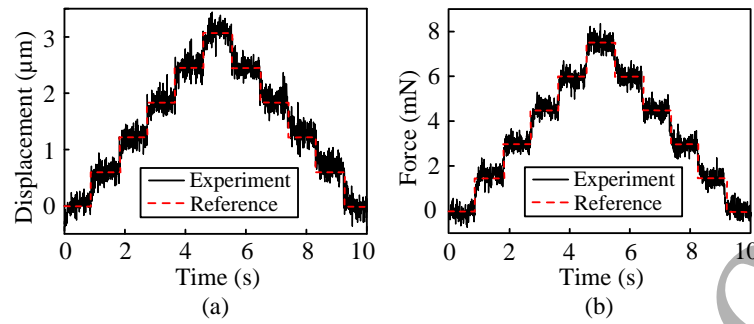


Figure 15. Resolution test results of (a) displacement and (b) force.

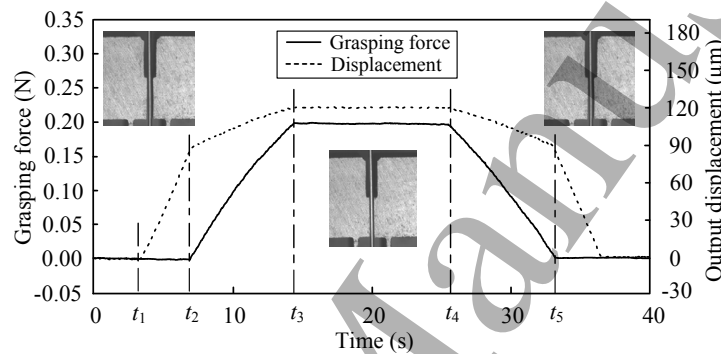


Figure 16. Test results of the micromanipulator for pick-hold-release operation of a metal wire by the first-stage end-effector.

dual-stage grasping characteristic as well as a large-sized object manipulation of the micromanipulator, Fig. 17 shows the grasping process of the more thinner and thicker metal wires with the diameter of about $100\ \mu\text{m}$ and $800\ \mu\text{m}$ by the first- and second-stage end-effector, respectively. The above experiments indicate the great potential of the developed micromanipulator in micro/nano manipulation and assembly tasks.

To evaluate the dynamic performance of the developed micromanipulator, a sinusoidal swept voltage signal with a 0.2-V p-p value and a frequency ranging from 10 Hz to 800 Hz is applied to the SPCA and the output displacement is recorded. The dynamic response of the micromanipulator is shown in Fig. 18, from the time- and frequency-domain point of view. It is seen that the first two resonance frequencies are 105.9 Hz and 119.8 Hz, which coincide with the simulation results of 115.2 Hz and 125.2 Hz, respectively. It is known that a low resonance frequency can limit the control bandwidth of the system. Thus, the developed micromanipulator can be used only for the low-speed object manipulation and assembly tasks.

5.3. Performance Comparison and Future Work

For a clear comparison, the performance parameters of several typical SPCA-actuated micromanipulators are summarized in Table 3. It can be seen from Table 3 that the developed micromanipulator can provide a larger MAR and operation range

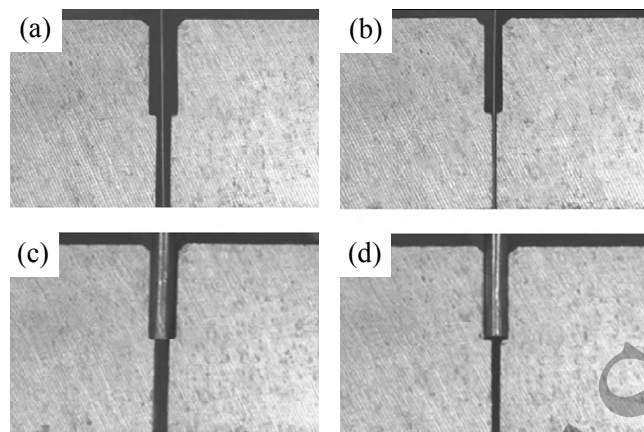


Figure 17. Grasping process of a metal wire with a diameter of (a)-(b) 100 μm and (c)-(d) 800 μm by the first- and second-stage end-effector respectively.

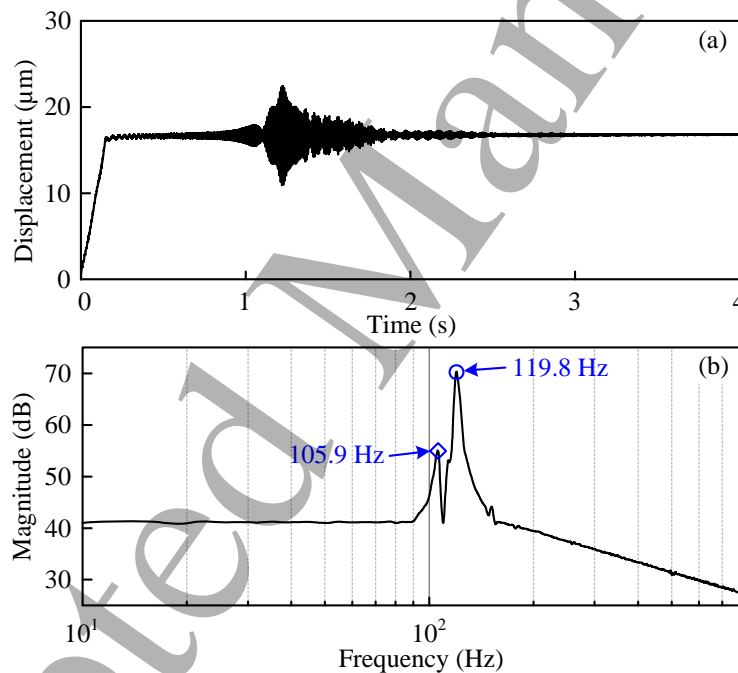


Figure 18. Dynamic response of the micromanipulator: (a) time-domain analysis and (b) frequency-domain analysis.

around 3 ~ 6 times that of others besides high displacement/force resolution.

In the future work, the hybrid position and force control of the micromanipulator will be implemented to conduct some complex manipulation tasks. Structural optimization will be also performed to achieve a more compact and much larger-range micromanipulator. Moreover, the micromanipulator can be attached to a robot arm with high positioning accuracy (e.g., UR 5 with a positioning accuracy of ± 0.1 mm far less than the operation range of the micromanipulator, from Universal Robots, Inc) to extend the operation space for practical industrial applications.

Table 4. Performance comparison with several typical SPCA-actuated micromanipulators

Reference	Displacement resolution (μm)	Force resolution (mN)	Frequency (Hz)	MAR	Operation range (μm)
[2]	0.23	1.001	244	14.8	280
[5], [26]	0.4	0.37	942	11.4	190
[22]	1.08	0.954	341.1	16	240
[24]	0.547	4.72	326.8	11.5	163.3
This work	0.6	1.8	105.9	58.8	1000

^aNote that the MAR in Table 3 is the ratio of half of the grasping range to the input displacement.

6. Conclusion

Design, modeling, simulation, and experimental tests of a novel SPCA-actuated micromanipulator is presented in this paper. To achieve a large grasping range, the micromanipulator structure is designed with a three-stage FMAM and a two-stage grasping end-effector. Based on the PRBM approach, the kinematics, statics and dynamics analysis are carried out. FEA simulation and experimental tests are conducted to evaluate the performance and verify the effectiveness of the developed micromanipulator. The conclusions of this paper are summarized as follows:

1) Three improved SR mechanisms are first proposed, and they have a larger MAR relative to the original one. Two of those have negligible coupling rates, therefore can serve as a linear guiding module in robotic mechanisms.

2) A concept of the multi-stage grasping end-effector is introduced, and the operation range of the end-effector will be N times as large as that of the single-stage one (N is the pair number of the end-effector jaws) without the assistance of any FMAMs.

3) The micromanipulator possesses built-in strain-gauge position and force sensors, which increases the integration level, and enables a miniature and compact structure.

4) The micromanipulator has a millimeter-scale grasping range with $0.6\text{-}\mu\text{m}$ displacement and 1.8-mN force resolution, and a large out-of-plane stiffness of $26.3\text{ mN}/\mu\text{m}$, which enables the operation of most micro objects with different physical properties in terms of size, fragility, and weight.

Acknowledgments

This work is supported by National Natural Science Foundation of China under Grant Nos. 51275018 and 51475017. The authors thank the reviewers for their professional comments and suggestions to improve the quality of this paper.

References

- [1] A. A. Ramadan, T. Takubo, Y. Mae, K. Oohara, et. al, Development process of a chopstick-like hybrid-structure two-fingered micromanipulator hand for 3-D manipulation of microscopic

- objects, IEEE Transactions on Industrial Electronics, 56(4), pp. 1121-1135, 2009.
- [2] Q. Xu, Design and smooth position/Force switching control of a miniature gripper for automated microhandling, IEEE Transactions on Industrial Informatics, 10(2), pp. 1023-2031, 2014.
 - [3] A. Ferreira, J. Agnus, N. Chaillet, J. M. Breguet, A smart microrobot on chip: design, identification, and control, IEEE/ASME Transactions on Mechatronics, 9(3), pp. 508-519, 2004.
 - [4] R. Zhang, J. Chu, and H. Wang, A multipurpose electrothermal microgripper for biological micro-manipulation, Microsystem Technologies, 19(1), pp.89-97, 2013.
 - [5] F. Wang, C. Liang, Y. Tian, X. Zhao, and D. Zhang, Design and control of a compliant microgripper with a large amplification ratio for high-Speed micro manipulation, IEEE/ASME Transactions on Mechatronics, 21(3), pp. 1262-1271, 2016.
 - [6] D. H. Kim, M. G. Lee, B. Kim, and Y. Sun, A superelastic alloy microgripper with embedded electromagnetic actuators and piezoelectric force sensors: a numerical and experimental study, Smart Materials and Structures, 14, pp.1265-72, 2005.
 - [7] M. N. M. Zubir and B. Shirinzadeh, Development of a high precision flexure-based microgripper, Precision Engineering, 33(4), pp. 362-370, 2009.
 - [8] M. N. M. Zubir, B. Shirinzadeh A, Y. Tian, A new design of piezoelectric driven compliant-based microgripper for micromanipulation, Mechanism and Machine Theory, 44(12), pp. 2248-2264, 2009.
 - [9] H. R. Cheong, C. Y. Teo, P. L. Leow, and K. C. Lai, Wireless-powered electroactive soft microgripper, Smart Materials and Structures, 27(5), pp. 055014, 2018.
 - [10] X. Zhang and Q. Xu, Design and testing of a novel 2-DOF compound constant-force parallel gripper, Precision Engineering, online, 2018.
 - [11] T. Chen, L. Chen, L. Sun, and X. Li, Design and fabrication of a four-arm-structure MEMS gripper, IEEE Transactions on Industrial Electronics, 56(4), pp. 996-1003, 2009.
 - [12] M. Boudaoud, Y. Haddab, and Y. L. Gorrec, Modeling and optimal force control of a nonlinear electrostatic microgripper, IEEE/ASME Transactions on Mechatronics, 18(3), pp. 1130-1139, 2013.
 - [13] Q. Xu, Design, fabrication, and testing of an MEMS microgripper with dual-axis force sensor, IEEE Sensors Journal, 15(10), pp. 6017-6026, 2015.
 - [14] R. Zhang, J. Chu, H. Wang, and Z. Chen, A multipurpose electrothermal microgripper for biological micro-manipulation, Microsystem Technologies, 19, pp. 8997, 2013.
 - [15] J. Chu, R. Zhang, and Z. Chen, A novel SU-8 electrothermal microgripper based on the type synthesis of the kinematic chain method and the stiffness matrix method, Journal of Micromechanics and Microengineering, 21, pp. 054030, 2011.
 - [16] Q. Xu, Design and development of a novel compliant gripper with integrated position and grasping/interaction force sensing, IEEE Transactions on Automation Science and Engineering, 14(3), pp. 1415-1428, 2017.
 - [17] G. Hao, and R. B. Hand, Design and static testing of a compact distributed-compliance gripper based on flexure motion, Archives of Civil and Mechanical Engineering, 16, pp. 708-716, 2016.
 - [18] Q. Xu, A novel compliant micropositioning stage with dual ranges and resolutions, Sensors and Actuators A: Physical, 205, pp. 6-14, 2014.
 - [19] D. Kang, K. Kim, D. Kim, J. Shim, D. G. Gweon, and J. Jeong, Optimal design of high precision XY-scanner with nanometer-level resolution and millimeter-level working range, Mechatronics, 19(4), pp. 562570, 2009.
 - [20] C. C. Lan, C. M. Lin, and C. H. Fan, A self-sensing microgripper module with wide handling ranges, IEEE/ASME Transactions on Mechatronics, 16(1), pp. 141-150, 2011.
 - [21] Z. W. Zhong and C. K. Yeong, Development of a gripper using SMA wire, Sensors Actuators A: Physical, 126, pp. 375381, 2006.
 - [22] D. H. Wang, Q. Yang, and H. M. Dong, A monolithic compliant piezoelectric-driven microgripper: design, modeling, and testing, IEEE/ASME Transactions on Mechatronics, 18(1), pp. 138-147, 2013.

- [23] Y. Yang, Y. Wei, J. Lou, F. Xie, and L. Fu, Development and precision position/force control of a new flexure-based microgripper, *Journal of Micromechanics and Microengineering*, 26, pp. 015005, 2016.
- [24] W. Chen, J. Qu, W. Chen, and J. Zhang, A compliant dual-axis gripper with integrated position and force sensing, *Mechatronics*, 47, pp. 105-115, 2017.
- [25] D. Zhang, Z. Zhang, Q. Gao, D. Xu, and S. Liu, Development of a monolithic compliant SPCA-driven micro-gripper, *Mechatronics*, 25, pp. 37-43, 2015.
- [26] F. Wang, C. Liang, Y. Tian, X. Zhao, and D. Zhang, Design of a piezoelectric-actuated microgripper with a three-Stage flexure-based amplification, *IEEE/ASME Transactions on Mechatronics*, 20(5), pp. 2205-2013, 2015.
- [27] K. Kim, X. Liu, Y. Zhang, and Y. Sun, Nanonewton force-controlled manipulation of biological cells using a monolithic MEMS microgripper with two-axis force feedback, *Journal of Micromechanics and Microengineering*, 18(5), pp. 055103, 2008.
- [28] Y. Wei, and Q. Xu, An overview of micro-Force sensing techniques, *Sensors and Actuators A: Physical*, 234, pp. 359-374, 2015.
- [29] B. Piriyanont and S. O. R. Moheimani, MEMS rotary microgripper with integrated electrothermal force sensor, *Journal of Microelectromechanical Systems*, 23(6), pp. 12491251, 2014.
- [30] B. Komati, C. Clevy, Member, and P. Lutz, High bandwidth microgripper with integrated force sensors and position estimation for the grasp of multi-stiffness microcomponents, *IEEE/ASME Transactions on Mechatronics*, 21(4), pp. 2039-2049, 2016.
- [31] M. Ohka, Y. Mitsuya, I. Higashioka, and H. Kabeshita, An experimental optical three-axis tactile sensor for micro-Robots, *Robotica*, 23, pp. 457-465, 2005.
- [32] Y. Liu, Y. Zhang, and Q. Xu, Design and control of a novel compliant constant-Force gripper based on buckled fixed-guided beams, *IEEE/ASME Transactions on Mechatronics*, 22(1), pp. 476-486, 2017.
- [33] D. J. Cappelleri, G. Piazza, and V. Kumar, A two dimensional vision-based force sensor for microrobotic applications, *Sensors and Actuators A: Physical*, 171, pp. 340-351, 2011.
- [34] A. Punning, M. Kruusmaa, and A. Aabloo, A self-sensing ion conducting polymer metal composite (IPMC) actuator, *Sensors and Actuators A: Physical*, 136(2), pp. 656664, 2007.
- [35] A. S. Putra, S. Huang, K. K. Tan, S. K. Panda, and T. H. Lee, Self-sensing actuation with adaptive control in applications with switching trajectory, *IEEE/ASME Transactions on Mechatronics*, 13(1), pp. 104-111, 2008.
- [36] H. Tang and Y. Li, Development and active disturbance rejection control of a compliant micro-/nanopositioning piezostage with dual mode, *IEEE Transactions on Industrial Electronics*, 61(3), pp. 1475-1492.
- [37] T. Na, J. Choi, J. Jung, H. Kim, J. Han, K. Park, and I. Oh, Compact piezoelectric tripod manipulator based on a reverse bridge-type amplification mechanism, *Smart Materials and Structures*, 25, pp. 095028, 2016.
- [38] K. B. Choi, J. J. Lee, and S. Hata, A piezo-driven compliant stage with double mechanical amplification mechanisms arranged in parallel, *Sensors and Actuators A: Physical*, 161, pp. 173-181, 2010.
- [39] W. Zhu, Z. Zhu, Y. Shi, X. Wang, K. Guan, and B. Ju, Design, modeling, analysis, and testing of a novel piezo-actuated XY compliant mechanism for large workspace nanopositioning, *Smart Materials and Structures*, 25, pp. 115033-18, 2016.
- [40] Y. Tian, B. Shirinzadeh, D. Zhang, and G. Alici, Development and dynamic modelling of a flexure-based Scott-Russell mechanism for nano-manipulation, *Mechanical Systems and Signal Processing*, 23, pp. 957-978, 2009.
- [41] Y. Qin, B. Shirinzadeh, D. Zhang, and Y. Tian, Design and kinematics modeling of a novel 3-DOF monolithic manipulator featuring improved Scott-Russell mechanisms, *Journal of Mechanical Design*, 135, pp. 10100409, 2013.
- [42] G. Hao, X. Kong, and R. L. Reuben, A nonlinear analysis of spatial compliant parallel modules:

1
2
3
4
5
6
7
8
9
10
11
12
13
14
15
16
17
18
19
20
21
22
23
24
25
26
27
28
29
30
31
32
33
34
35
36
37
38
39
40
41
42
43
44
45
46
47
48
49
50
51
52
53
54
55
56
57
58
59
60

IOP Publishing, Smart Materials and Structures, 2019

25

Multi-beam modules, Mechanism and Machine Theory, 46, pp. 680-706, 2011.

Accepted Manuscript